Graphical Abstract

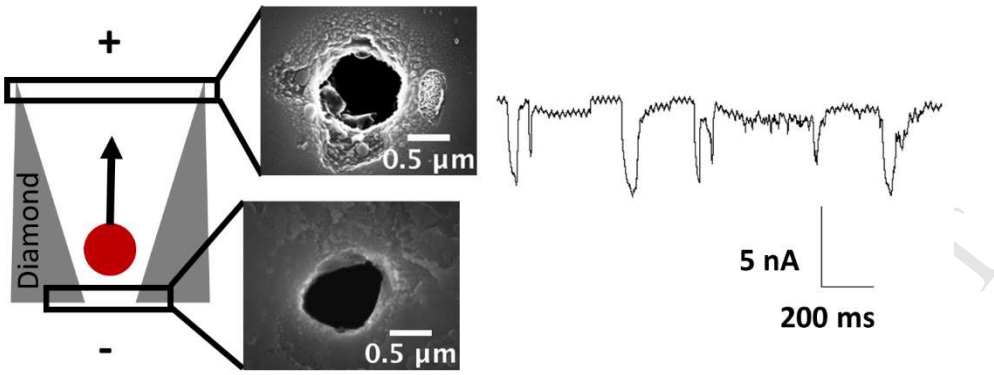

We demonstrate for the first-time fabrication of a sub-micron pore which spans the entirety of a single crystal diamond membrane and investigate the impact of this new pore material on particle translocation.

Fabrication of a Single Sub-Micron Pore Spanning a Single Crystal (100) Diamond Membrane and Impact on Particle Translocation

Jennifer R. Webb,[a] Aiden A. Martin,[b,c] Robert P. Johnson,[d,e] Maxim B. Joseph,[d] Mark E. Newton,[f] Igor Aharonovich,[c] Milos Toth[c] and Julie V. Macpherson[*d]

a. MOAC Doctoral Training Centre, University of Warwick Coventry, CV4 7AL, UK.

b. Lawrence Livermore National Laboratory, Livermore, California 94550, USA

c. School of Mathematical and Physical Sciences, University of Technology, Sydney, Ultimo, NSW 2007, Australia.

d. Department of Chemistry, University of Warwick, Coventry, CV4 7AL, UK.

e. School of Chemistry, University of Lincoln, Lincoln, LN6 7TS

f. Department of Physics, University of Warwick, Coventry, CV4 7AL, UK

Fabrication of sub-micron (meso)pores in single crystal diamond membranes, which span the entirety of the membrane, is described for the first time, and the translocation properties of polymeric particles through the pore investigated. The pores are produced using a combination of laser micromachining to form the membrane and electron beam induced etching to form the pore. Single crystal diamond as the membrane material, has the advantages of chemical stability and durability, does not hydrate and swell, has outstanding electrical properties that facilitate fast, low noise current-time measurements and is optically transparent for combined optical-conductance sensing. The resulting pores are characterized individually using both conductance measurements, employing a microcapillary electrochemical setup, and electron microscopy. Proof-of-concept experiments to sense charged polystyrene particles as they are electrophoretically driven through a single diamond pore are performed, and the impact of this new pore material on particle translocation is explored. These findings reveal the potential of diamond as a platform for pore-based sensing technologies and pave the way for the fabrication of single nanopores which span the entirety of a diamond membrane.

Submitted to “Nanocarbons for electrochemistry” special issue, **March 2017; revised May 2017**

* Email: j.macpherson@warwick.ac.uk; +44 2476 573886

1. Introduction

Detecting events at the single particle (and ultimately molecule) level on very short time scales is a fundamental challenge in the scientific community. One approach to the problem is the use of solid-state micropores, which span a membrane, i.e. thru-holes, as employed in traditional Coulter counters (sub-micron to millimeter sized pores).[1, 2] More recently, nanopores have been utilised.[3]

Pore based sensors operate in real-time and rely on the measurement of changes in conduction current as the analyte (particle or molecule) passes through the pore. The amplitude, shape, duration and frequency of each translocation event can provide unique information about an individual analyte such as size, speed and relative population.[4] The dimension of the smallest constriction of the pore controls the maximum size of molecules/particles that can pass through for detection. Highly sensitive electronics allows detection of very small changes in the conduction current, facilitating high-resolution size discrimination. The simplicity of the concept linked with the versatility of the method has led to the use of solid-state pores for a wide range of applications involving micro- and nano-sized particles,[5-9] polymer chains[10] and proteins.[11-14]

The capability of the technology to facilitate rapid and direct evaluation of individual DNA bases has made it particularly attractive for next-generation DNA sequencing.[15-18] However, a high noise level during high frequency, low current measurements, continues to be a general limitation of nanopore technology that still requires addressing. One potential approach, recently pioneered by Long and co-workers, is to simultaneously collect optical measurements, which do not suffer from flicker noise, with electrical measurements as analytes pass through a nanopore.[19-21] The choice of substrate material in which the pore is placed is critical for the stability and sensing capability of the device, including the noise level. In order to facilitate low noise and fast data acquisition experiments over the widest

range of analytes the material should ideally have: (i) a high electrical resistivity and low dielectric constant; (ii) chemical stability in a wide range of solvents and; (iii) must be amenable to processing such that pores of a known geometry can be reproducibly fabricated at the single pore level.

To-date various materials have been employed to produce micro- and nano- pores, including silicon nitride,[22, 23] glass,[24] aluminum oxide,[25] graphene, [26-28] and track etched polymer foils,[29, 30] using a range of fabrication methodologies, typically involving electron beam or focused ion beam (FIB) milling.[31] The length of the pore is often an important consideration, for example for sequencing of long chain molecules such as DNA, single-base discrimination requires high spatial resolution that can be provided by low aspect ratio pores,[3] such as atomically thin graphene.[26, 27] In contrast, investigation of pore-particle translocation dynamics is suited to pores where the length is greater than that of the analyte to facilitate enhanced time resolution and longer event signals.[32, 33] Consideration of the platform material and fabrication methodology is therefore crucial to fabricate pores of appropriate dimensions for analyte detection.

One material that has received little attention to-date but has properties which make it ideal for micro- and nano- pore particle translocation measurements is diamond. Diamond is chemically stable and durable offering extremely high resistance to chemical attack in strong acid and alkali solutions,[34] allowing treatments to be applied to clean the pore without changing the geometry or degrading the structure. This is highly advantageous because as the pores get smaller in size devices often fail due to analytes irreversibly blocking the pore.[35]

Moreover, diamond surfaces are not prone to hydration “swelling” phenomenon, as found with silicate-based structures, e.g. glass and quartz,[36] which change the geometrical properties of the pore. Diamond is also robust, amenable to microfabrication techniques, and can be easily modified between hydrophilic (O-terminated) and hydrophobic (H-terminated)

surface functionalization for enhanced chemical selectivity.[37, 38] Furthermore, the optical transparency of diamond offers the potential for dual optical-conductance sensing.[39]

In single crystal form, diamond has a very high resistivity in the insulating state (10^{13} – 10^{16} Ωcm), a very low dielectric constant (5.7) and a low dielectric loss tangent (< 1 x 10^{-5} at 30 – 150 GHz),[40, 41] making it near ideal for fast, low noise current-time measurements compared to other materials. This means diamond should not require further surface modification to reduce overall dielectric noise, unlike materials such as silicon nitride, which often require coating with materials such as polydimethylsiloxane.[42]

There are no reports in the literature for the formation of individual micro- or nano- pores which span a single crystal diamond membrane. Pores have been made in diamond by annealing nickel (or carbon soluble metal) nanoparticles on the surface to locally remove carbon and produce etch pits. However, the pores do not span the entirety of the diamond film and the pore density is often very high.[43-46] Masuda and coworkers reported a method for the fabrication of sub-micron thru-hole pores in polycrystalline diamond using oxygen plasma etching.[47] However, the dense array produced rendered the material microporous making it unsuitable for particle translocation studies. Furthermore, polycrystalline diamond is far from ideal, compared to single crystal diamond, due to its inferior electrical properties, reduced physical properties as a result of grain boundaries and impaired performance of optical defects.[48] Moreover, contamination from amorphous and sp^2 carbon, often inherent in polycrystalline diamond unless growth conditions are carefully controlled, will increase the capacitance of the diamond causing increased dielectric noise in particle transduction measurements.[49]

In this paper, we demonstrate a new methodology for the fabrication of a single sub-micron thru-hole pore in a freestanding single crystal diamond membrane, and show how this structure can be employed to investigate polymeric particle translocation. Moreover, the

resulting current-time traces can also be used to provide information on the internal properties of the pore.

2. Experimental

2.1 Solutions

All solutions were prepared using Milli-Q water (Millipore Corp., UK) with a resistivity of 18.2 MΩ at 25 °C that was filtered through a 0.22 μm syringe filter (Millex® filter units, Millipore Corp). 0.1 M KCl (Sigma-Aldrich, USA) solutions were prepared for electrochemical characterization of the diamond pores. For the particle translocation experiments, polystyrene (PS) particles of mean 800 nm diameter (Sigma-Aldrich, USA) were dispersed in filtered 0.01 M KCl solution (pH 6.9) containing 0.1 % Triton X-100 to prevent particle self-aggregation (Sigma-Aldrich, US) at a concentration of 107 particles ml^{-1}. The diamond was cleaned prior to use in boiling concentrated sulfuric acid (98% H_2SO_4; Sigma Aldrich, US) supersaturated with KNO_3 (Fischer Scientific, UK).[50] Individual pores were cleaned in situ by cycling a potential across the pore between −2 and +2 V in 0.5 M $HClO_4$ (Sigma-Aldrich, MO, USA).

2.2 Diamond Pore Fabrication

The starting substrate was a single crystal (100) diamond plate (Element Six, Harwell, UK), 4.38 mm × 4.48 mm and 50 μm ± 3 μm thick, grown using high pressure, high temperature conditions and polished to < 5 nm roughness on both sides (Element Six, Harwell, UK). Using a laser micromachiner (E-355H-3-ATHI-O, Oxford Lasers, UK, 532 nm laser wavelength, beam size ~ 3 μm), the diamond was thinned down to ~ <5 μm thickness in sixteen evenly spaced ~ 180 μm diameter circular regions. Due to the high transparency of the insulating diamond surface, black glass pen was applied evenly to the upper diamond

surface to ensure the laser pulse energy was maximally absorbed. This enabled the diamond to be ablated evenly rather than fracturing or being otherwise uncontrollably damaged. A higher laser power (15 % attenuation) was required for the initial cut of the diamond surface, while a lower power (5 % attenuation) was sufficient to cut a surface that had already been partially ablated. Hence, the laser power was reduced after the first pass and for all subsequent passes to maximize the *z*-resolution of the thinning technique.

To maximize the regularity of ablation, the pitch between pulses and lines of pulses were the same (3 µm or ½ of the laser spot size) and the stage speed was kept slow enough (0.3 mm s^{-1}) so that no significant acceleration/deceleration artefacts were observed. A laser frequency of 100 Hz was employed to ensure that the pitch between pulses was 3 µm. To keep the laser spot in focus, for ideal laser ablation, the focal position was moved downwards in line with the depth of material removed with each pass. This depth was monitored by white light interferometry (WLI) profiling of the ablated structures after several passes (Contour GT, Bruker, UK). The final diamond membrane was imaged using a polarized optical microscope (Olympus BH2-HLSH).

Pores were fabricated using electron beam induced etching (EBIE) and the entrance side imaged using an FEI Nova NanoSEM variable pressure[51] field emission - scanning electron microscope (FE-SEM) equipped with a magnetic field-assisted gaseous secondary electron detector (GSED).[52] The FE-SEM chamber was filled with water (Milli-Q) vapour to a pressure of 13 Pa to mediate EBIE and suppress charging of the electrically insulating diamond surface. Prior to EBIE, the diamond substrate was coated *ex situ* with a ~ 30 nm graphitic carbon coating to further suppress surface charging during electron irradiation. This minimized diffusion of the e-beam and enabled pattern control during the time scale of the irradiation. The pores investigated in this study were fabricated using a stationary 15 keV, 24 nA electron beam. The pore diameter could be varied by changing the focal distance of the

electron beam relative to the surface, thus controlling the electron irradiation area on the diamond.

2.3 Diamond Pore Characterization

Pore cross-sectioning was achieved using focused ion beam (FIB) milling (JEOL 4500 FIB/SEM, JEOL). The pore was slowly exposed by progressive vertical slicing using a 5 kV, 10 nC μm^{-2} focused beam of positively charged Ga^{+} ions, and monitored *in situ* by backscattered electron (BSE) imaging using a 20 keV electron beam positioned at an angle of 53° relative to the FIB beam. High-resolution images of the EBIE exit side and diamond pore cross-section were acquired using FE-SEM (Zeiss Supra 55 VP, Zeiss). For both systems, an in-lens detector was used at electron beam energy between 10 and 20 keV with a working distance of 4 mm. The average depth of each trench was determined using WLI (Contour GT, Bruker, UK) and the pore entrance-exit areas were measured using pixel thresholding with ImageJ software (US National Institutes of Health).

2.4 Solution Conductance Measurements

The custom-built holder was designed in SolidWorks (Dassault Systémes, FR) and fabricated by micro-stereolithography (MSL) by photo cross-linking commercial R11 resin using a Perfactory Mini Multi-Lens system (Envisiontec, DE). The holder was designed with three essential features; (i) a central hole fabricated to the exact dimensions of the diamond substrate with a thin 100 μm deep recess for the substrate to slot into; (ii) a circular reservoir with inlet/outlet channels to allow back-filling with solution and removal of any air bubbles beneath the substrate; and (iii) a side channel for insertion of a AgCl-coated Ag wire (Ag/AgCl), serving as a quasi-reference counter electrode (QRCE), into the reservoir solution. The base of the MSL cell was sealed with optically clear quartz to allow visual monitoring of

air bubble formation within the reservoir. All components were sealed in place using epoxy adhesive to ensure a leak-free device. The reservoir was filled with solution so that all sixteen pores in the diamond single crystal substrate were wetted from the pore exit side.

Current-voltage, *i-V* responses were measured using a potentiostat (CHI730A, CH Instruments Inc., US) connected to a desktop computer. Current – time, *i-t* responses were recorded at a sampling frequency of 100 kHz using a home-built current collector with a virtual bandwidth of 10 kHz connected to the computer via a data acquisition (DAQ) card (NI PCIe-6259, National Instruments, UK). Data were recorded using custom-built LabVIEW code (LabVIEW 2014, National Instruments, UK). Potentials are defined with the outside of the pore as ground. It was not necessary to filter the data, which we attribute to both the use of a grounded Faraday cage which isolated the system from external sources of noise and the low high-frequency capacitance that is intrinsic to the diamond substrate[53]. The low noise - a standard deviation of just 0.2 nA in the baseline current was observed - highlights the potential that diamond has as a substrate for ion-channel recordings.

2.5 Particle Characterization

The hydrodynamic diameters of the PS particles were determined by dynamic light scattering (DLS) using a Malvern Zetasizer NanoS, and captured by FE-SEM (Zeiss Supra 55 VP) using a 2 keV electron beam and a type II secondary electron (SE2) detector.

2.6 Signal Processing and Simulations

The *i-t* traces were analyzed using the freeware package QUB (v2.0023). The start and end points of each event were identified as the first inflection points either side of the peak, and the local baseline (i_{base}) was defined around each event by averaging ± 500 data points either side of the start and end. This method eliminates long-time drift which we attribute to

solution evaporation and can be reduced using a humidity cell in future experiments. The peak current, Δi, was defined as the difference between the maximum current blockade during the particle translocation event and the immediate baseline. Events were filtered so that only those with a prominent height greater than 2 nA (i.e., 10× the standard deviation of the baseline) and having a characteristic asymmetric current signature (indicative of translocation through a conical pore [54]) were analysed. A high threshold was used in our analysis due to particle-pore interactions that did not result in complete translocation of the particle. These non-translocation events were short (<20 ms) and/or with Δi less than 2 nA in magnitude (*vide infra*). Finite element method (FEM) simulations were performed using COMSOL Multiphysics 4.4 (COMSOL AB, SE).

2. Results & Discussion

3.1 Diamond Membrane Formation

Prior to thru-pore formation, it was necessary to fabricate a thin (< 5 µm thick) diamond membrane in the starting single crystal diamond substrate (50 µm thick), as outlined in Figure 1a. The starting material was thus laser micromachined and depth control during thinning was achieved by modulating the frequency, stage speed, attenuator percentage and the pitch between the lines and laser pulses, as described in more detail in the experimental section. In total sixteen isolated circular trenches of diameter ~ 180 µm were fabricated on the substrate, as shown in Figure 1b. The average membrane thickness was 1.9 – 4.4 µm with a roughness 1 – 2 µm, (inner face) and < 5 nm (polished outer face), as measured by WLI. A typical FE-SEM image of a lasered circular trench is shown in Figure 1c. Here, the rastered cross-hatch pattern formed by several laser passes can be clearly observed. Figure 1d displays a WLI

cross-section of an ablated trench, the undulations on the inner surface produced by the laser path are clearly evident.

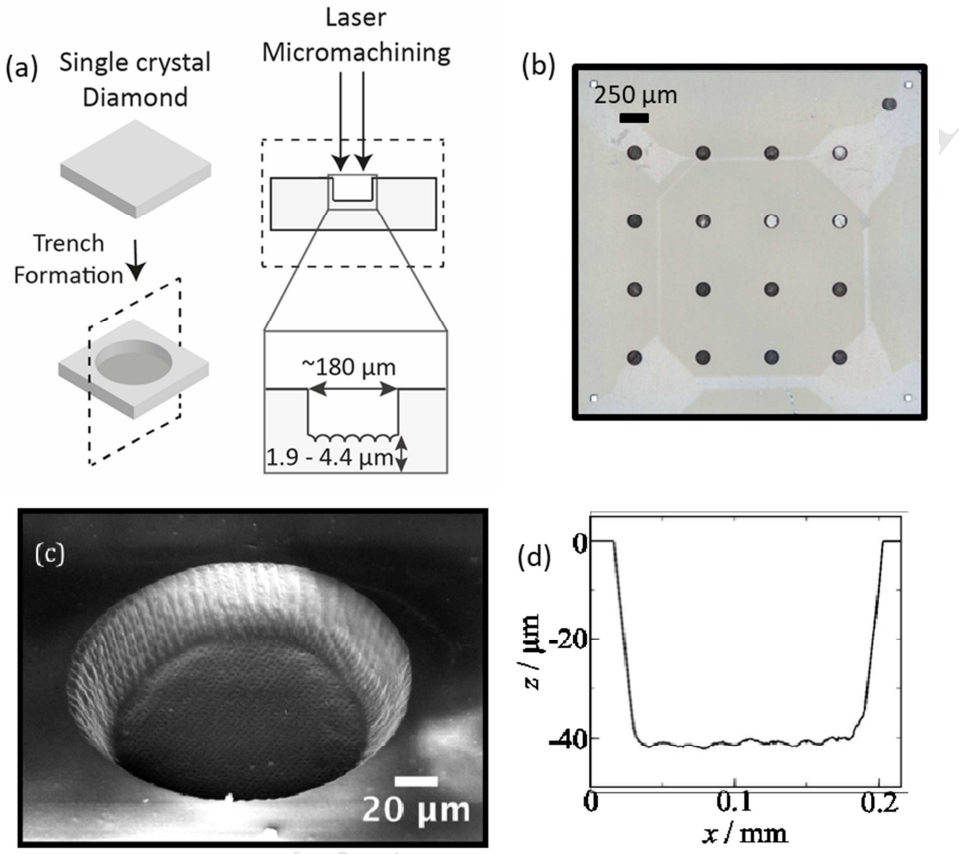

Figure 1: Fabrication of an array of thin, circular membranes supported in a single crystal (100) diamond substrate using laser micromachining: (a) Illustration of the laser micromachining procedure. (b) Optical image of a single crystal diamond membrane after creation of sixteen trenches for subsequent pore insertion (center) and one for sample alignment (top right). (c) Characterization of a single lasered trench by FE-SEM displaying the rastered cross-hatch laser path and (d) WLI cross-sectioning of lateral *x*- vs. depth *z*- dimensions to assess surface roughness.

3.2 Diamond Pore Formation

A single pore was inserted into each trench using gas-mediated EBIE [55, 56] as illustrated in Figure 2a. EBIE is a nanoscale, direct-write technique. The main advantage of EBIE over conventional electron-beam or FIB milling is the elimination of sputtering, material graphitization and ion implantation during processing, as well as greater material

selectivity.[57] The method proceeds through a dry-chemical process where gaseous precursor molecules (here, H_2O) decompose on the diamond surface leading to oxygen termination. Simultaneously, the surface is irradiated by an electron beam which breaks C–C bonds resulting in desorption of a surface carbon and oxygen atom as CO, leaving a void in the substrate.[58, 59] This procedure is simpler than current methodologies that typically involve several preparatory stages and post-fabrication modifications.[60]

The diamond membrane was mounted on a silicon substrate. Pore formation was monitored using *in situ* endpoint detection[61] by measuring the GSED output voltage during etching, as shown in Figure 2b. The GSED voltage initially drops as etch pit formation initiates, and electrons are contained wholly within the diamond membrane (Figure 2bi). As the electron beam penetrates into the underlying silicon, the GSED output voltage increases (Fig. 2bii), until diamond material is completely etched in the region irradiated by the electron beam, and the GSED output voltage saturates (Fig. 2biii).

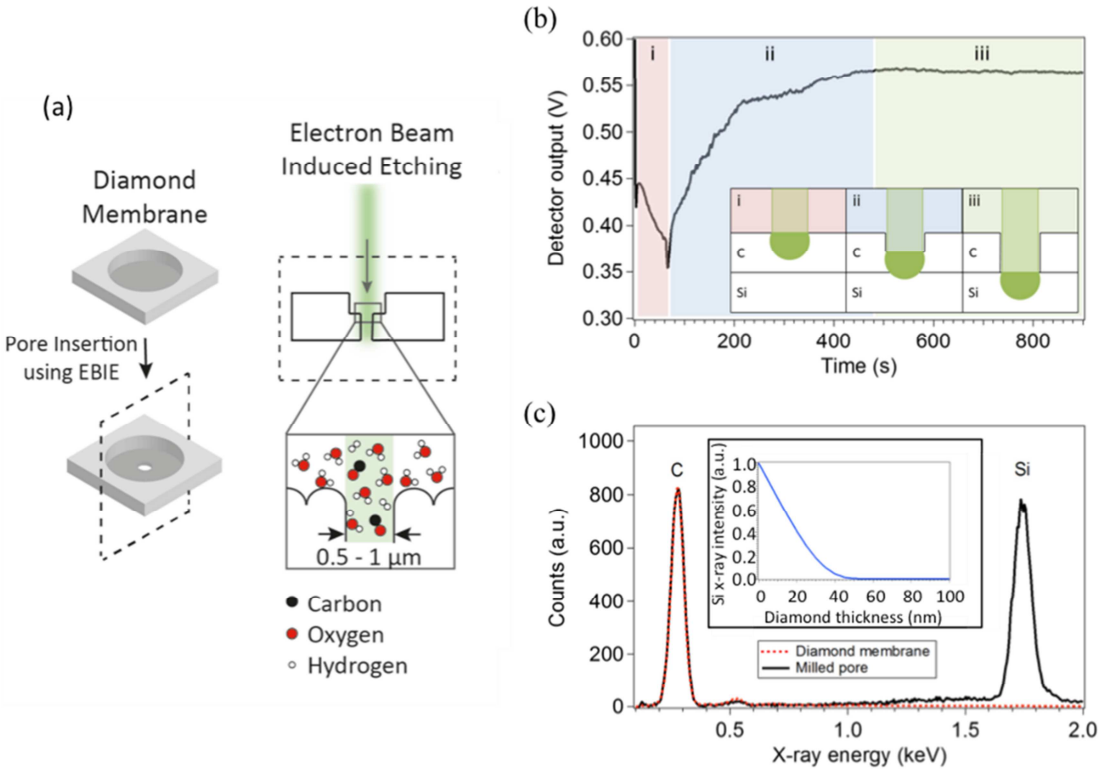

Fig. 2 Single crystal diamond pore fabrication using water-mediated electron beam induced etching (EBIE): (a) Illustration of the fabrication procedure. (b) *In situ* endpoint

monitoring of pore formation during EBIE. (c) EDS spectra acquired using a 3 keV electron beam. When the electron beam irradiates a pore-free diamond membrane (-) no signal from the underlying silicon is detected, however when the pore (-) is irradiated, silicon X-rays are detected. Inset: Intensity of X-rays generated in the underlying silicon as a function of diamond layer thickness simulated for a 3 keV electron beam using the Monte Carlo package CASINO.

After etching, the pores were characterized *in situ* in the FE-SEM by energy-dispersive X-ray spectroscopy (EDS) to also confirm formation (Figure 2c). At low electron beam energies, the depth at which X-rays are generated in the material is very shallow. For diamond placed flat on a silicon substrate, when the thickness of diamond is less than the electron penetration range and the electron beam energy is greater than the critical ionization energy (Si K 1s = 1.84 keV),[62] X-rays will be generated in the underlying silicon.

The intensity of the generated X-rays was determined as a function of diamond thickness at an electron beam energy of 3 keV, using the Monte Carlo simulation package CASINO.[63] The simulations show X-rays are generated in the underlying silicon when the diamond thickness is less than ~ 50 nm (Fig. 2c inset). Hence, X-ray spectra measured using a 3 keV electron beam can be used to show with confidence that etch pits in diamond have been milled down to at least 50 nm from the underlying silicon. When the fabricated pores were examined by EDS using a 3 keV electron beam, all pores exhibited a detectable silicon X-ray signal. EDS examination of both a non-lasered region of the diamond substrate and a pore-free membrane did not reveal any detectable silicon X-ray signal.

Further confirmation was made using conventional FE-SEM to image both surfaces of the pore containing membrane. Figure 3ai and ii show typical FE-SEM images of the EBIE formed entrance (inner lasered surface of membrane) and exit (pristine single

crystal outer surface of membrane) apertures, respectively. Further images are presented in ***Electronic Supporting information, ESI 1***. The entrance-exit FE-SEM images (of 42 pores in total) were all in the range of 0.5 – 1.0 μm diameter. This data highlights that the EBIE method can produce individual sub-micron sized thru-pores in single crystal diamond membranes with fairly reproducible entrance-exit size characteristics.

The dimensions of three representative EBIE pores are detailed in Table 1. Pore 1 corresponds to Figure 3a, and pore 2 to ***ESI 1***, Fig. S1a. Typically, the EBIE entrance aperture (diameter) is only very slightly larger than the exit aperture (diameter), measured using pixel thresholding (Table 1). To elucidate the sub-surface pore geometry, a cross-section of an EBIE diamond pore (of thickness 12.5 μm) within an isolated trench was created using FIB milling, as shown in Figure 3bi. The cross-section in Figure 3bii displays a slight conical geometry. This shape, we believe is as a consequence of the EBIE etching mechanism. Pore geometry is governed by the electron beam profile at the vacuum-membrane surface interface. The focal point of the electron beam during EBIE irradiation was fixed 50 μm below the pristine diamond membrane surface. Therefore, as diamond material is removed the receding surface of the etch pit gets closer to the electron beam focal point, resulting in a small reduction in the electron beam diameter at the vacuum-surface interface. Very slight broadening can also occur at the EBIE exit due to the scattered electrons penetrating through the exit giving rise to material removal outside the primary irradiation area. The conical shape of the pore allows us to term the entrance the “base” and the exit the “tip”, in line with conical pore nomenclature.

Table 1 Comparison of the predicted size of four diamond pores calculated from solution conductance and microscopy data.

Pore	Membrane Thickness (L) [μm][a]	Inner membrane surface roughness (rms) [μm][a]	Diameter of pore entrance (base) [nm][b]	Diameter of pore exit (tip) [nm][b]	Experimental Current @ + 1 V [μA][c]	Theoretical Current @ + 1 V [μA][d]

1.	3.0 ± 0.5	0.50	789.7 ± 15.5	777.6 ± 10.0	0.17	0.17 ± 0.05
2	3.5 ± 0.6	0.64	729.6 ± 17.9	714.5 ± 19.7	0.15	0.13 ± 0.04
3.	2.0 ± 0.8	0.82	450.5 ± 9.1	440.2 ± 16.4	0.09	0.08 ± 0.04

a) Measured by interferometry with rms roughness; b) Measured from FE-SEM images; c) Obtained from *i-V* response in Figure 4d; d) Calculated using FEM.

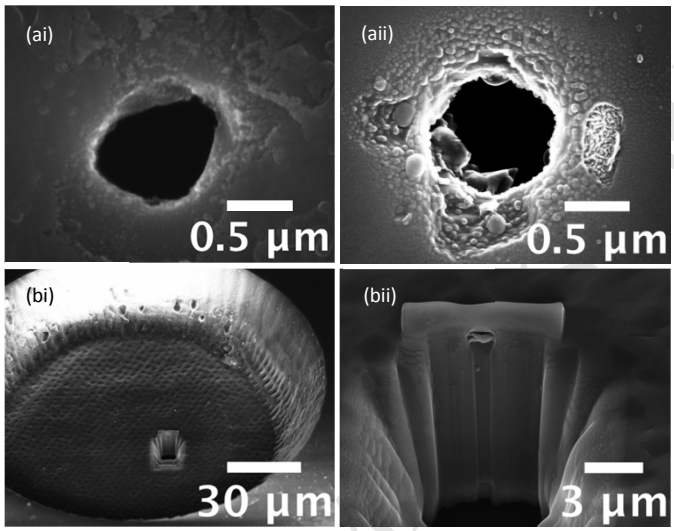

Figure 3: (a) FE-SEM images of EBIE of diamond membrane thru-pore 1 (in Table 1); (i) entrance and (ii) exit apertures; (b) FE-SEM images of (i) the lasered trench from which an individual pore was accessed by FIB milling and (ii) a magnified version of the resulting pore cross-section obtained displaying high aspect ratio characteristics.

3.3 Conductance measurements using diamond pores

Individual pore solution conductance was measured using a microcapillary setup,[64] (Figure 4) and the substrate was mounted in a custom-built cell fabricated by MSL, as described in the experimental section.[65] In order to electrochemically interrogate an individual pore the microcapillary electrochemical method,[64] as illustrated in Figure 4b, was used to deliver solution to an individual diamond trench (and hence single pore) and electrically connect the circuit by providing a second QRCE. Briefly, a glass borosilicate capillary was pulled and polished to an inner diameter of 200 µm. The microcapillary and holder reservoir were filled initially with a 0.1 M KCl solution and an Ag/AgCl QRCE

was inserted into the microcapillary channel. The microcapillary was positioned using *x-y-z* micropositioners and a high magnification camera, so that the meniscus wetted an entire circular trench, as shown in Figure 4c. All measurements were made in a two-electrode setup where a voltage was applied between the Ag/AgCl QRCEs placed either side of the diamond substrate to facilitate ionic conductance current through the pore. By simply repositioning the microcapillary over individual trenches it was possible to make ion conductance measurements on a pore-by-pore basis.

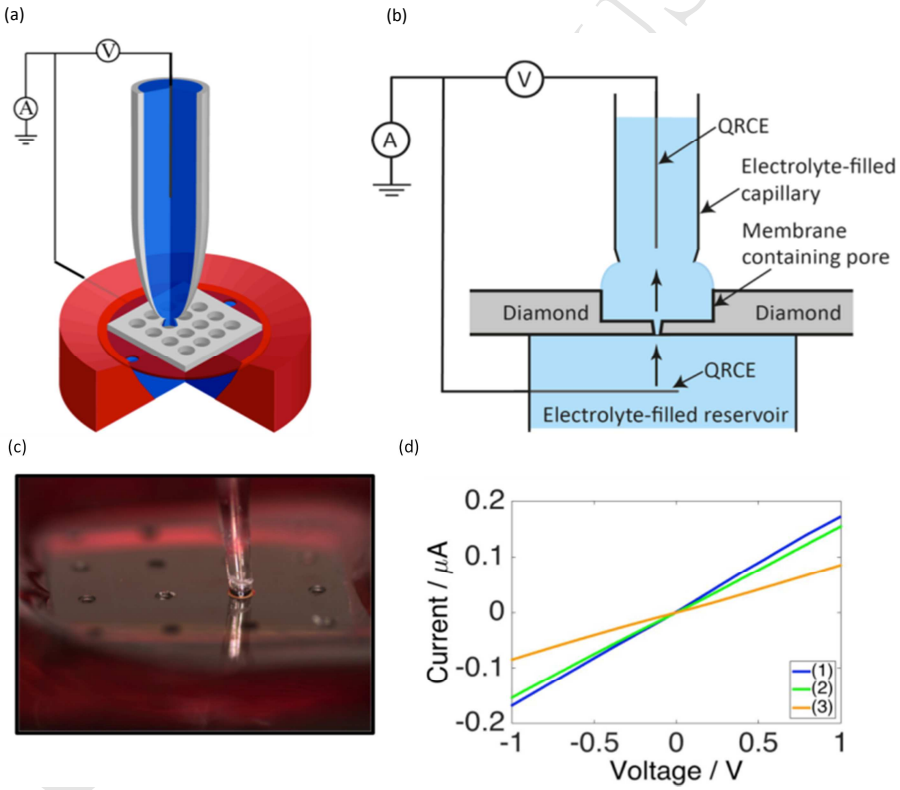

Figure 4: (a) Schematic of the microelectrochemical set-up for diamond pore experiments. The diamond membrane was mounted in a specialized holder and a ~200 μm outer diameter glass microcapillary, filled with the solution of interest, was positioned so that the meniscus wetted an individual trench containing a single diamond pore. (b) Illustration of the large-scale microcapillary method for single pore investigation. A potential is applied between two Ag/AgCl electrodes positioned to drive a conductance current through the pore. (c) Optical image of the solution meniscus from the large

microcapillary in contact with the diamond membrane. (d) *i-V* curves from three single crystal diamond pores of varying size (see Table 1) fabricated by EBIE.

The current-voltage (*i-V*) characteristics in the ±1 V range for three independent diamond pores (labelled 1 – 3 in Table 1), fabricated by EBIE are shown in Figure 4d. All pores displayed linear *i-V* responses with no evidence of ionic current rectification[66, 67] or electrostatic gating[68], as expected for pores of this larger (~ μm) size. FEM simulations were employed to match the observable pore geometry to the theoretical *i-V* response. Details of the model are discussed in ***ESI 2***. In brief, each pore was modelled simply as a cylinder with a very small conical angle, based on the measured average entrance-exit diameters (assuming circular geometry for both apertures) and trench thickness, as detailed in Table 1. The expected conductance current at an applied potential of +1 V was determined and compared to the corresponding experimental *i-V* response at that potential (Table 1). Close agreement was observed between the predicted and experimental current through the different sized diamond pores, which shows the model employed adequately describes the internal pore geometry.

3.4 Polystyrene Particle Translocation

To assess the detection capability of the diamond pores, PS particles were electrophoretically driven through an individual pore (pore 1, Table 1), using an applied voltage of +200 mV. Note for the applied voltage polarity the PS particles move from the tip (EBIE exit) to the base (EBIE entrance). The negatively charged PS particles of zeta potential ~ -30 mV at the electrolyte pH 6.9[69] displayed a size distribution of 800 ± 470 nm as measured by DLS (***ESI 3***).

Individual peaks were observed in the *i-t* responses that were not observed in the conductance trace in the absence of particles, shown in Figure 5a. Figure 5b shows the

resulting *i-t* trace of PS particles as they interact with the diamond pore. In both the presence and absence of particles, a drift in the measured current base line (increasing ~ 0.5 nA min^{-1}) is observed. This is most probably a consequence of evaporation from the high surface area to volume droplet, positioned in contact with the solution-filled pore. Future implementation of a controlled humidity cell would likely mitigate against this drift.[64] The high aspect ratio of the pore (length of ~ 3 μm and diameter of ~780 nm i.e. thickness-to-diameter aspect ratio of ~ 3.9) facilitates enhanced time resolution and longer event signals, allowing the observation of greater detail within events that can elucidate different particle dynamics. Figure 5bi – iii display zoom-ins of typical particle event types.

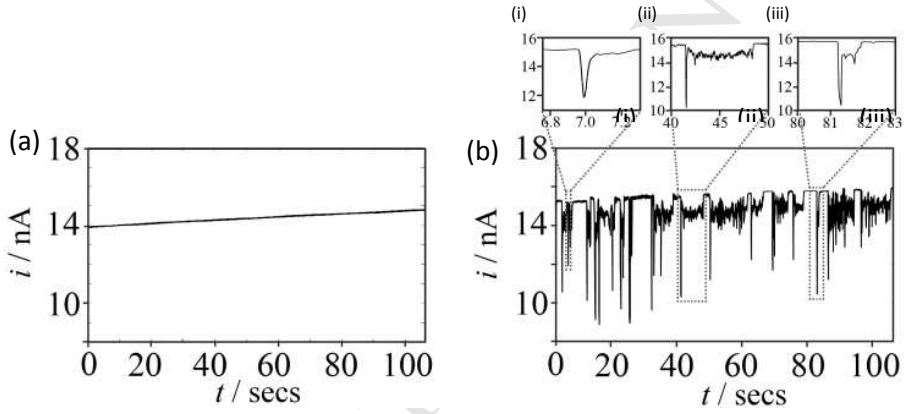

Figure 5: Event analysis of PS particles interacting with a diamond pore: *i-t* traces (a) in the absence of particles, displaying no blockade events, and (b) on addition of PS particles with three frequently occurring particle blockade events displayed in (i) – (iii). Drift in the open-pore baseline was observed due to solution evaporation and can be reduced using a humidity cell in future experiments. For the purpose of this work, the drift was inconsequential for the PS translocation studies.

All events display a characteristic pulse, often followed by a tail which relates to the pore-particle interactions. The difference in the length and shape of events in the *i-t* trace indicates different particle dynamics within the pore and different particle sizes in the

solution. For all translocation events, the magnitude of the current peak (Δi) relates to particle size. The different pore-particle event types possible in our system (translocation, trapping, rebound and blockage) are shown schematically in Figure 6.

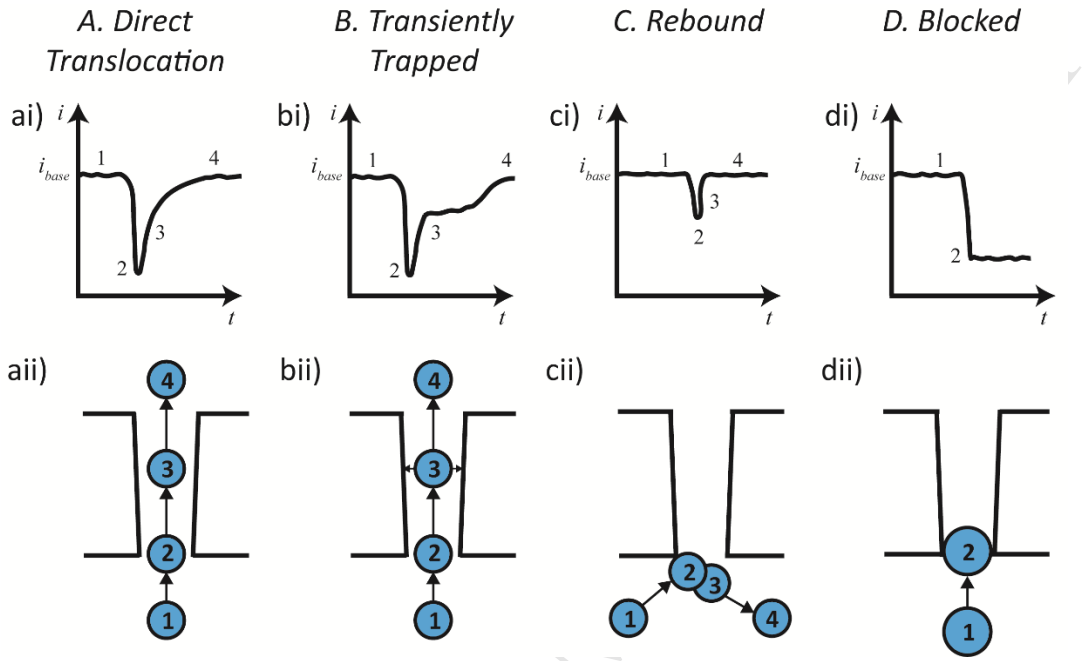

Figure 6: Different particle-pore events a – d where (i) display the representative *i-t* trace and (ii) is an illustration of the corresponding pore-particle interaction. Four main event categories exist: (a) Direct translocation of a particle; (b) Translocation of a particle which becomes transiently trapped within the channel during travel; (c) Rebound pore-particle interaction. The decrease in current is highly dependent on the angle at which the particle impacts with the pore and is of lower magnitude than translocation-type events; (d) Complete pore blockage by a particle of comparable size to the pore. Events consist of (1) baseline pore current prior to an event, (2) decrease in current due to particle blocking the pore opening, (3) increase in pore current as the particle moves away from the pore opening, and (4) pore current returning back to baseline post-event. Not to scale.

Four main categories of blockade event were observed: (a) Direct translocation, where the particle travels through the diamond pore without interacting with the walls. The current rapidly drops in magnitude (by between 3 – 8 nA) due to the particle displacing electrolyte solution; the largest volume of solution is displaced at the smallest constriction

in the pore. Upon exiting the pore the current returns to the baseline value (this is the largest current value measured, the current spikes from baseline refer to a decrease in the current signal); (b) Hindered translocation, where the particle interacts with the walls of the diamond pore during translocation causing it to become transiently trapped within the channel. This produces current fluctuations beyond the peak current that relate to binding and detachment of the particle[32] within the diamond channel. The shape relates to the internal structure of the pore, especially with smaller particles that can achieve higher spatial resolution resulting in more distinctive tail fluctuations; (c) Pore-particle rebound where the particle interacts with or near to the pore aperture but rebounds back into the bulk solution instead of entering. The magnitude of the current block is small, typically 0.2-1 nA from the baseline and of short (< 20 ms) duration; (d) Complete blockage, where the particle becomes permanently stuck in the pore causing the current to drop indefinitely. This event type was not observed during the course of our experiments. The above categorizations enable qualitative and semi-quantitative interpretation of the different event types.

We analysed events only with direct translocation-type signatures (Figure 6ai) to determine the peak current (Δi) and particle translocation time (Figure 7). Events which show a $\Delta i$of 2 nA or greater, i.e., a minimum of 10× greater than the standard deviation in the baseline current, are attributed to translocation. Analyses were performed for migration of the negatively charged polystyrene particles in both directions through the pore, i.e. tip (EBIE exit) to base (entrance) (+mV) and base to tip (-mV). Translocation times were found to be 57 ± 4 ms at -200 mV and 56 ± 1 ms at +200 mV, indicating the translocation time (t) is independent of travel direction through the pore. The peak current (Δi), however, was found to be dependent on the direction of travel. An average peak height of 7.7 ± 0.1 nA was observed when the particles migrated from base to tip , while

an average of 5.3 ± 0.1 nA was observed when particles migrated in the opposite direction (tip to base).

A previous study of particle transport through conical, charged polyethylene terephthalate pores of a similar size to those employed here, attributed a directional dependence on the peak current, to voltage-regulated ionic concentrations within the pore.[70] In particular, for a negatively charged pore and negatively charge particle, a greater blocking peak current is observed when the particle travels from the tip to base. With the diamond pore, the opposite effect is observed, for a negatively charged particle the greater peak blocking current is observed for particle travel from base to tip (Figure 7). Given that the asymmetry is driven by ion accumulation/depletion effects as a result of the charge on the pore walls, we tentatively speculate that the internal walls of the diamond pore are positively, not negatively, charged. This could be as a result of possible graphitization during the EBIE fabrication process. Graphitization of diamond particles has been previously shown to result in positive surface charges at neutral pH.[71, 72]

The *i-t* traces recorded for tip (EBIE exit) to base (EBIE entrance) translocation and vice-versa are not perfect mirror images of one another. This could indicate the pore is not symmetrical about its through-pore axis (Figure 3), and/or may contain variations in internal wall charges as a result of the fabrication process.

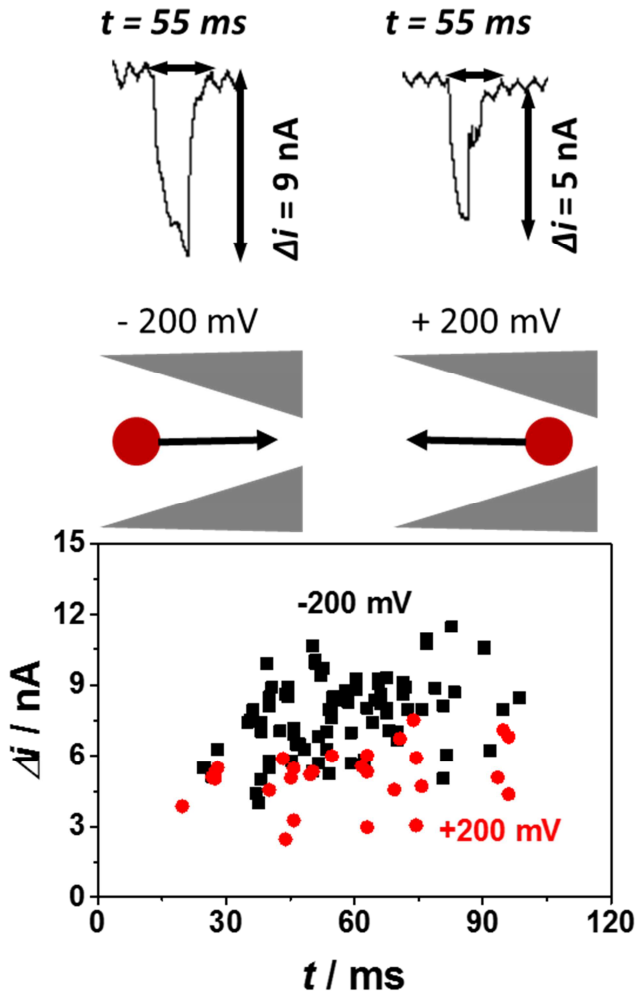

Fig 7. Analysis of translocation-type events (Fig 6ai) under either a +200 mV or -200 mV applied potential. The distribution of peak current (Δi) and transient times (t) for an ensemble of individually measured particles were found to be Gaussian-like (Fig. S4).

3. Conclusions

We have shown, for the first time, the fabrication of a single sub-micron sized thru-pore in a single crystal diamond membrane and successfully monitored particle translocation through the pore using PS particles and solution conductance measurements. The pores were fabricated using a two-step process which involved laser thinning to produce a ~ 1.9 – 4.4 μm thin membrane and then EBIE to expose a single pore, which spans the entirety of the membrane. The pores were characterized using both FE-SEM and conductance measurements and shown to exhibit reproducible characteristics that match well to theory.

The translocation capabilities of the diamond pore were investigated using PS particles. Low noise *i-t* traces were achievable without the requirement for noise filtering or surface modification, which can in part be attributed to the low high-frequency capacitance intrinsic to the diamond substrate.[53] Furthermore, the high aspect ratio (~3.9) of the pores allowed sufficient time resolution to observe detailed particle dynamics based on the interactions of the PS particles with the diamond pore. Analysis of asymmetric resistive pulses, of a type similar to those previously reported for conical glass pores, and indicative of translocating particles, reported translocation times (in the range 56 – 57 ms) independent of the direction of travel through the pore. In contrast, the peak currents showed a strong dependence on the direction of particle travel.

While further work is required before the inherent stability and other benefits of diamond can be realized in a pore device this work marks the first step towards reliably fabricating a sub-micron thru-pore from diamond. For example, it should be possible to eliminate drift in the base line (due to evaporation effects) and fluctuations in the base line response (potentially due to inadequate shielding) by improving the experimental setup.[73-75] From a fabrication standpoint, it is envisaged using refinements to the EBIE process or alternative etching techniques, smaller sized (~10's of nms) pores would

be possible in the single crystal diamond membrane. Etching techniques could also be used to form the starting membrane.[76] Furthermore, with layered diamond growth, it is possible to produce single crystal devices which have conducting diamond grown on top of insulating diamond.[77] This makes it then possible to build in electric-field enhancement [78, 79] capabilities that could facilitate analyte detection into the single-nucleotide base resolution.

Acknowledgments. JRW acknowledges funding for a studentship from the Engineering and Physical Sciences Research Council through the MOAC Doctoral Training Centre (grant number EP/F500378/1). JVM thanks the Royal Society for the award of an Industry Fellowship. RPJ acknowledges funding from a Marie Curie International Outgoing Fellowship under the EU FP7 program (Project No. 625984). The EBIE aspect of this work was funded by FEI Company. A portion of this work was performed under the auspices of the U.S. Department of Energy by Lawrence Livermore National Laboratory under Contract DE-AC52-07NA27344. AAM is the recipient of a John Stocker Postgraduate Scholarship from the Science and Industry Endowment Fund. IA is the recipient of an Australian Research Council Discovery Early Career Research Award (Project Number DE130100592).

Appendix A: Supplementary Information. (1) FE-SEM images of EBIE-fabricated single crystal diamond pores; (2) FEM simulation of ionic current blockades through a pore; (3) Particle characterization by DLS and FE-SEM and (4) Particle translocation analysis.

References

[1] R. DeBlois, C. Bean, Counting and sizing of submicron particles by the resistive pulse technique, Rev. Sci. Instrum. 41(7) (1970) 909-916.
[2] H. Bayley, C.R. Martin, Resistive-pulse sensing from microbes to molecules, Chem. Rev. 100(7) (2000) 2575-2594.
[3] C. Dekker, Solid-state nanopores, Nat. Nanotechnol. 2(4) (2007) 209-215.
[4] S. Howorka, Z. Siwy, Nanopore analytics: sensing of single molecules, Chem. Soc. Rev. 38(8) (2009) 2360-2384.
[5] J. Kong, H. Wu, L. Liu, X. Xie, L. Wu, X. Ye, Q. Liu, Silicon Nitride Nanopores for Nanoparticle Sensing, J. Nanosci. Nanotechnol. 13(6) (2013) 4010-4016.
[6] W.-J. Lan, D.A. Holden, B. Zhang, H.S. White, Nanoparticle transport in conical-shaped nanopores, Anal. Chem. 83(10) (2011) 3840-3847.
[7] K. Venta, M. Wanunu, M. Drndić, Electrically Controlled Nanoparticle Synthesis inside Nanopores, Nano Lett. 13(2) (2013) 423-429.
[8] Y. Astier, L. Datas, R. Carney, F. Stellacci, F. Gentile, E. DiFabrizio, Artificial Surface‐Modified Si3N4 Nanopores for Single Surface‐Modified Gold Nanoparticle Scanning, Small 7(4) (2011) 455-459.
[9] R. Vogel, G. Willmott, D. Kozak, G.S. Roberts, W. Anderson, L. Groenewegen, B. Glossop, A. Barnett, A. Turner, M. Trau, Quantitative sizing of nano/microparticles with a tunable elastomeric pore sensor, Anal. Chem. 83(9) (2011) 3499-3506.
[10] P. Rowghanian, A.Y. Grosberg, Force-driven polymer translocation through a nanopore: An old problem revisited, J. Phys. Chem. B 115(48) (2011) 14127-14135.
[11] E.C. Yusko, J.M. Johnson, S. Majd, P. Prangkio, R.C. Rollings, J. Li, J. Yang, M. Mayer, Controlling protein translocation through nanopores with bio-inspired fluid walls, Nat. Nanotechnol. 6(4) (2011) 253-260.
[12] D.S. Talaga, J. Li, Single-molecule protein unfolding in solid state nanopores, J. Am. Chem. Soc. 131(26) (2009) 9287-9297.
[13] C. Plesa, J.W. Ruitenberg, M.J. Witteveen, C. Dekker, Detection of individual proteins bound along DNA using solid state nanopores, Nano Lett. (2015).
[14] D. Japrung, J. Dogan, K.J. Freedman, A. Nadzeyka, S. Bauerdick, T. Albrecht, M.J. Kim, P. Jemth, J.B. Edel, Single-molecule studies of intrinsically disordered proteins using solid-state nanopores, Anal. Chem. 85(4) (2013) 2449-2456.
[15] A.J. Storm, C. Storm, J. Chen, H. Zandbergen, J.-F. Joanny, C. Dekker, Fast DNA translocation through a solid-state nanopore, Nano Lett. 5(7) (2005) 1193-1197.
[16] S.W. Kowalczyk, M.W. Tuijtel, S.P. Donkers, C. Dekker, Unraveling single-stranded DNA in a solid-state nanopore, Nano Lett. 10(4) (2010) 1414-1420.
[17] D. Fologea, J. Uplinger, B. Thomas, D.S. McNabb, J. Li, Slowing DNA translocation in a solid-state nanopore, Nano Lett. 5(9) (2005) 1734-1737.
[18] U.F. Keyser, B.N. Koeleman, S. Van Dorp, D. Krapf, R.M. Smeets, S.G. Lemay, N.H. Dekker, C. Dekker, Direct force measurements on DNA in a solid-state nanopore, Nat. Phys. 2(7) (2006) 473-477.
[19] Y. Cao, Y. Lin, R.-C. Qian, Y.-L. Ying, W. Si, J. Sha, Y. Chen, Y.-T. Long, Evidence of single-nanoparticle translocation through a solid-state nanopore by plasmon resonance energy transfer, Chem. Comm. 52(30) (2016) 5230-5233.

[20] X. Shi, R. Gao, Y.-L. Ying, W. Si, Y.-F. Chen, Y.-T. Long, A Scattering Nanopore for Single Nanoentity Sensing, ACS Sensors 1(9) (2016) 1086-1090.
[21] X. Shi, R. Gao, Y.-L. Ying, W. Si, Y. Chen, Y.-T. Long, An integrated system for optical and electrical detection of single molecules/particles inside a solid-state nanopore, Faraday Discussions 184(0) (2015) 85-99.
[22] A. Storm, J. Chen, X. Ling, H. Zandbergen, C. Dekker, Fabrication of solid-state nanopores with single-nanometre precision, Nat. Mater. 2(8) (2003) 537-540.
[23] K. Briggs, H. Kwok, V. Tabard‐Cossa, Automated Fabrication of 2‐nm Solid‐State Nanopores for Nucleic Acid Analysis, Small 10(10) (2014) 2077-2086.
[24] B. Zhang, J. Galusha, P.G. Shiozawa, G. Wang, A.J. Bergren, R.M. Jones, R.J. White, E.N. Ervin, C.C. Cauley, H.S. White, Bench-top method for fabricating glass-sealed nanodisk electrodes, glass nanopore electrodes, and glass nanopore membranes of controlled size, Anal. Chem. 79(13) (2007) 4778-4787.
[25] F. Li, L. Zhang, R.M. Metzger, On the Growth of Highly Ordered Pores in Anodized Aluminum Oxide, Chemistry of Materials 10(9) (1998) 2470-2480.
[26] C.A. Merchant, K. Healy, M. Wanunu, V. Ray, N. Peterman, J. Bartel, M.D. Fischbein, K. Venta, Z. Luo, A.C. Johnson, DNA translocation through graphene nanopores, Nano Lett. 10(8) (2010) 2915-2921.
[27] G.F. Schneider, S.W. Kowalczyk, V.E. Calado, G. Pandraud, H.W. Zandbergen, L.M. Vandersypen, C. Dekker, DNA translocation through graphene nanopores, Nano Lett. 10(8) (2010) 3163-3167.
[28] M.D. Fischbein, M. Drndić, Electron beam nanosculpting of suspended graphene sheets, Applied Physics Letters 93(11) (2008) 113107.
[29] A. Mara, Z. Siwy, C. Trautmann, J. Wan, F. Kamme, An asymmetric polymer nanopore for single molecule detection, Nano Lett. 4(3) (2004) 497-501.
[30] P.Y. Apel, I.V. Blonskaya, S.N. Dmitriev, O.L. Orelovitch, A. Presz, B.A. Sartowska, Fabrication of nanopores in polymer foils with surfactant-controlled longitudinal profiles, Nanotechnol. 18(30) (2007) 305302.
[31] K. Healy, B. Schiedt, A.P. Morrison, Solid-state nanopore technologies for nanopore-based DNA analysis, Nanomedicine 2(6) (2007) 875-897.
[32] M. Pevarnik, K. Healy, M.E. Toimil-Molares, A. Morrison, S.E. Létant, Z.S. Siwy, Polystyrene particles reveal pore substructure as they translocate, ACS Nano. 6(8) (2012) 7295-7302.
[33] D. Kozak, W. Anderson, R. Vogel, S. Chen, F. Antaw, M. Trau, Simultaneous size and ζ-potential measurements of individual nanoparticles in dispersion using size-tunable pore sensors, ACS Nano 6(8) (2012) 6990-6997.
[34] R. Ramesham, M. Rose, Electrochemical characterization of doped and undoped CVD diamond deposited by microwave plasma, Diam. Relat. Mater. 6(1) (1997) 17-26.
[35] M. Wanunu, Nanopores: A journey towards DNA sequencing, Phys. Life Rev. 9(2) (2012) 125-158.
[36] R.K. Iler, The Chemistry of Silica, Wiley, New York1979.
[37] H.V. Patten, L.A. Hutton, J.R. Webb, M.E. Newton, P.R. Unwin, J.V. Macpherson, Electrochemical “read–write” microscale patterning of boron doped diamond electrodes, Chem. Comm. 51(1) (2015) 164-167.
[38] L.A. Hutton, J.G. Iacobini, E. Bitziou, R.B. Channon, M.E. Newton, J.V. Macpherson, Examination of the factors affecting the electrochemical performance of oxygen-terminated polycrystalline boron-doped diamond electrodes, Anal. Chem. 85(15) (2013) 7230-7240.

[39] W.H. Pitchford, H.-J. Kim, A.P. Ivanov, H.-M. Kim, J.-S. Yu, R.J. Leatherbarrow, T. Albrecht, K.-B. Kim, J.B. Edel, Synchronized optical and electronic detection of biomolecules using a low noise nanopore platform, ACS Nano 9(2) (2015) 1740-1748.
[40] S. Coe, R. Sussmann, Optical, thermal and mechanical properties of CVD diamond, Diam. Relat. Mater. 9(9) (2000) 1726-1729.
[41] J. von Windheim, V. Venkatesan, D. Malta, K. Das, Comparison of the electric properties of single-crystal and polycrystalline diamond by Hall effect and capacitance-voltage measurements, Diam. Relat. Mater. 2(5) (1993) 841-846.
[42] V. Tabard-Cossa, D. Trivedi, M. Wiggin, N.N. Jetha, A. Marziali, Noise analysis and reduction in solid-state nanopores, Nanotechnol. 18(30) (2007) 305505.
[43] H.-a. Mehedi, J.-C. Arnault, D. Eon, C. Hébert, D. Carole, F. Omnes, E. Gheeraert, Etching mechanism of diamond by Ni nanoparticles for fabrication of nanopores, Carbon 59 (2013) 448-456.
[44] W. Smirnov, J. Hees, D. Brink, W. Müller-Sebert, A. Kriele, O.A. Williams, C. Nebel, Anisotropic etching of diamond by molten Ni particles, Appl. Phys. Lett. 97(7) (2010) 073117.
[45] Y. Takasu, S. Konishi, W. Sugimoto, Y. Murakami, Catalytic formation of nanochannels in the surface layers of diamonds by metal nanoparticles, Electrochem. Solid St. 9(7) (2006) C114-C117.
[46] H.-A. Mehedi, C. Hébert, S. Ruffinatto, D. Eon, F. Omnès, E. Gheeraert, Formation of oriented nanostructures in diamond using metallic nanoparticles, Nanotechnol. 23(45) (2012) 455302.
[47] H. Masuda, K. Yasui, M. Watanabe, K. Nishio, M. Nakao, T. Tamamura, T.N. Rao, A. Fujishima, Fabrication of through-hole diamond membranes by plasma etching using anodic porous alumina mask, Electrochem. Solid St. 4(11) (2001) G101-G103.
[48] I. Aharonovich, A.D. Greentree, S. Prawer, Diamond photonics, Nat. Photonics 5(7) (2011) 397-405.
[49] E. Mahé, D. Devilliers, C. Comninellis, Electrochemical reactivity at graphitic micro-domains on polycrystalline boron doped diamond thin-films electrodes, Electrochim. Acta 50(11) (2005) 2263-2277.
[50] L.A. Hutton, J.G. Iacobini, E. Bitziou, R.B. Channon, M.E. Newton, J.V. Macpherson, Examination of the Factors Affecting the Electrochemical Performance of Oxygen-Terminated Polycrystalline Boron-Doped Diamond Electrodes, Analytical Chemistry 85(15) (2013) 7230-7240.
[51] G. Danilatos, Foundations of environmental scanning electron microscopy, Adv. Electron. Electron Phys. 71 (1988) 109-250.
[52] B. Thiel, M. Toth, R. Schroemges, J. Scholtz, G. van Veen, W. Knowles, Two-stage gas amplifier for ultrahigh resolution low vacuum scanning electron microscopy, Rev. Sci. Instrum. 77(3) (2006) 033705.
[53] J.A. von Windheim, V. Venkatesan, D.M. Malta, K. Das, Comparison of the electric properties of single-crystal and polycrystalline diamond by hall effect and capacitance-voltage measurements, Diamond and Related Materials 2(5) (1993) 841-846.
[54] W.-J. Lan, D.A. Holden, B. Zhang, H.S. White, Nanoparticle Transport in Conical-Shaped Nanopores, Analytical Chemistry 83(10) (2011) 3840-3847.
[55] J. Taniguchi, I. Miyamoto, N. Ohno, S. Honda, Electron beam assisted chemical etching of single crystal diamond substrates, Jpn. J. App. Phys. 35(12B) (1996) 6574-6578.
[56] J.-i. Niitsuma, X.-l. Yuan, S. Koizumi, T. Sekiguchi, Nanoprocessing of diamond using a variable pressure scanning electron microscope, Jpn. J. Appl. Phys. 45(1L) (2006) L71.

[57] M. Toth, C.J. Lobo, W.R. Knowles, M.R. Phillips, M.T. Postek, A.E. Vladár, Nanostructure fabrication by ultra-high-resolution environmental scanning electron microscopy, Nano Lett. 7(2) (2007) 525-530.
[58] A.A. Martin, M. Toth, I. Aharonovich, Subtractive 3D printing of optically active diamond structures, Sci. Rep. 4 (2014).
[59] A.A. Martin, A. Bahm, J. Bishop, I. Aharonovich, M. Toth, Dynamic Pattern Formation in Electron-Beam Induced Etching, Phys. Rev. Lett. 115 (2015) 255501.
[60] B.N. Miles, A.P. Ivanov, K.A. Wilson, F. Doğan, D. Japrung, J.B. Edel, Single molecule sensing with solid-state nanopores: novel materials, methods, and applications, Chem. Soc. Rev. 42(1) (2013) 15-28.
[61] I. Utke, P. Hoffmann, J. Melngailis, Gas-assisted focused electron beam and ion beam processing and fabrication, J. Vac. Sci. Tech. B 26(4) (2008) 1197-1276.
[62] J.B. Kortright, A.C. Thompson, X-ray Data Booklet, X-ray Data Booklet (2001).
[63] D. Drouin, A.R. Couture, D. Joly, X. Tastet, V. Aimez, R. Gauvin, CASINO V2. 42—A Fast and Easy‐to‐use Modeling Tool for Scanning Electron Microscopy and Microanalysis Users, Scanning 29(3) (2007) 92-101.
[64] T.M. Day, P.R. Unwin, J.V. Macpherson, Factors Controlling the Electrodeposition of Metal Nanoparticles on Pristine Single Walled Carbon Nanotubes, Nano Letters 7(1) (2007) 51-57.
[65] R.B. Channon, M.B. Joseph, J.V. Macpherson, Additive Manufacturing for Electrochemical (Micro)Fluidic Platforms, The Electrochemical Society Interface 25(1) (2016) 63-68.
[66] H.S. White, A. Bund, Ion current rectification at nanopores in glass membranes, Langmuir 24(5) (2008) 2212-2218.
[67] R. Karnik, C. Duan, K. Castelino, H. Daiguji, A. Majumdar, Rectification of ionic current in a nanofluidic diode, Nano Lett. 7(3) (2007) 547-551.
[68] H.S. White, A. Bund, Mechanism of electrostatic gating at conical glass nanopore electrodes, Langmuir 24(20) (2008) 12062-12067.
[69] D. Breite, M. Went, A. Prager, A. Schulze, Tailoring Membrane Surface Charges: A Novel Study on Electrostatic Interactions during Membrane Fouling, Polymers 7(10) (2015) 2017-2030.
[70] Y. Qiu, I. Vlassiouk, Y. Chen, Z.S. Siwy, Direction Dependence of Resistive-Pulse Amplitude in Conically Shaped Mesopores, Analytical Chemistry 88(9) (2016) 4917-4925.
[71] T. Petit, J.-C. Arnault, H.A. Girard, M. Sennour, T.-Y. Kang, C.-L. Cheng, P. Bergonzo, Oxygen hole doping of nanodiamond, Nanoscale 4(21) (2012) 6792-6799.
[72] N. Yang, Novel Aspects of Diamond, Springer International Publishing, Switzerland, 2015.
[73] Y. Lin, X. Shi, S.-C. Liu, Y.-L. Ying, Q. Li, R. Gao, F. Fathi, Y.-T. Long, H. Tian, Characterization of DNA duplex unzipping through a sub-2 nm solid-state nanopore, Chem. Comm. 53(25) (2017) 3539-3542.
[74] Y.-L. Ying, H.-Y. Wang, T.C. Sutherland, Y.-T. Long, Monitoring of an ATP-Binding Aptamer and its Conformational Changes Using an α-Hemolysin Nanopore, Small 7(1) (2011) 87-94.
[75] H.-Y. Wang, Y.-L. Ying, Y. Li, H.-B. Kraatz, Y.-T. Long, Nanopore Analysis of β-Amyloid Peptide Aggregation Transition Induced by Small Molecules, Analytical Chemistry 83(5) (2011) 1746-1752.

[76] M. Bonnauron, S. Saada, L. Rousseau, G. Lissorgues, C. Mer, P. Bergonzo, High aspect ratio diamond microelectrode array for neuronal activity measurements, Diam. Relat. Mater. 17(7) (2008) 1399-1404.
[77] L.I. Tomlinson, H.V. Patten, B.L. Green, J. Iacobini, K.E. Meadows, K. McKelvey, P.R. Unwin, M.E. Newton, J.V. Macpherson, Intermittent-contact Scanning Electrochemical Microscopy (IC-SECM) as a Quantitative Probe of Defects in Single Crystal Boron Doped Diamond Electrodes, Electroanalysis 28(10) (2016) 2297-2302.
[78] G.A. Chansin, R. Mulero, J. Hong, M.J. Kim, A.J. Demello, J.B. Edel, Single-molecule spectroscopy using nanoporous membranes, Nano Lett. 7(9) (2007) 2901-2906.
[79] A. Rutkowska, K. Freedman, J. Skalkowska, M.J. Kim, J.B. Edel, T. Albrecht, Electrodeposition and Bipolar Effects in Metallized Nanopores and Their Use in the Detection of Insulin, Anal. Chem. 87(4) (2015) 2337-2344.